Nano Research 2018, 11(4): 1834–1849
https://doi.org/10.1007/s12274-017-1801-2
Research Article
ISSN 1998-0124
CN 11-5974/O4

Electrical contacts in monolayer blue phosphorene devices

Jingzhen Li[1,§], Xiaotian Sun[3,§], Chengyong Xu[4,§], Xiuying Zhang[1], Yuanyuan Pan[1], Meng Ye[1], Zhigang Song[1], Ruge Quhe[5], Yangyang Wang[1,6], Han Zhang[1], Ying Guo[7], Jinbo Yang[1,2], Feng Pan[8] (✉), and Jing Lu[1,2] (✉)

[1] *State Key Laboratory for Mesoscopic Physics and Department of Physics, Peking University, Beijing 100871, China*
[2] *Collaborative Innovation Center of Quantum Matter, Beijing 100871, China*
[3] *College of Chemistry and Chemical Engineering, and Henan Key Laboratory of Function-Oriented Porous Materials, Luoyang Normal University, Luoyang 471934, China*
[4] *School of Science, Nanchang Institute of Technology, Nanchang 330099, China*
[5] *State Key Laboratory of Information Photonics and Optical Communications and School of Science, Beijing University of Posts and Telecommunications, Beijing 100876, China*
[6] *Nanophotonics and Optoelectronics Research Center, Qian Xuesen Laboratory of Space Technology, China Academy of Space Technology, Beijing 100094, China*
[7] *School of Physics and Telecommunication Engineering, Shaanxi University of Technology, Hanzhong 723001, China*
[8] *School of Advanced Materials, Peking University, Shenzhen Graduate School, Shenzhen 518055, China*
[§] *Jingzhen Li, Xiaotian Sun and Chengyong Xu contributed equally to this work.*

Received: 9 June 2017
Revised: 12 August 2017
Accepted: 13 August 2017

KEYWORDS

monolayer blue phosphorene, interface property, Schottky barrier, field-effect transistor, density functional theory, quantum transport simulation

ABSTRACT

Semiconducting monolayer (ML) blue phosphorene (BlueP) shares similar stability with ML black phosphorene (BP), and it has recently been grown on an Au surface. Potential ML BlueP devices often require direct contact with metal to enable the injection of carriers. Using *ab initio* electronic structure calculations and quantum transport simulations, for the first time, we perform a systematic study of the interfacial properties of ML BlueP in contact with metals spanning a wide work function range in a field effect transistor (FET) configuration. ML BlueP has undergone metallization owing to strong interaction with five metals. There is a strong Fermi level pinning (FLP) in the ML BlueP FETs due to the metal-induced gap states (MIGS) with a pinning factor of 0.42. ML BlueP forms n-type Schottky contact with Sc, Ag, and Pt electrodes with electron Schottky barrier heights (SBHs) of 0.22, 0.22, and 0.80 eV, respectively, and p-type Schottky contact with Au and Pd electrodes with hole SBHs of 0.61 and 0.79 eV, respectively. The MIGS are eliminated by inserting graphene between ML BlueP and the metal electrode, accompanied by a transition from a strong FLP to a weak FLP. Our study not only provides insight into the ML BlueP–metal interfaces, but also helps in the design of ML BlueP devices.

Address correspondence to Feng Pan, panfeng@pkusz.edu.cn; Jing Lu, jinglu@pku.edu.cn

1 Introduction

Owing to the excellent gate controllability related to their atomic thickness and the efficient transportation of carriers associated with few dangling bonds at the interface, two-dimensional (2D) semiconductors play an important role in the rapidly increasing global development of nanotechnology applications [1–3]. Black phosphorene (BP), which is an orthorhombic phase of phosphorene, has a high carrier mobility and a thickness-dependent direct band gap of around 0.30 (bulk)–1.00 (monolayer) eV at the generalized gradient approximation (GGA) of the density functional theory (DFT) level [4–6]. These properties make BP a potential novel 2D channel material in electronic and optoelectronic devices. In fact, BP field-effect transistors (FETs) with a large on/off ratio up to 10^5, a high mobility up to 1,000 $cm^2/(V{\cdot}s)$, and a broadband response to light ranging from the visible to the near-infrared region have been reported [7–9]. Blue phosphorene (BlueP), which is a hexagonal phase of phosphorene, is predicted to share similar stability with BP, and has an indirect thickness-dependent band gap of around 1.10 (bulk)–1.98 (monolayer) eV at the GGA of the DFT level [5, 10]. Recently, monolayer (ML) BlueP has been grown on the Au surface, and its semiconductor property is confirmed experimentally [11]. Accordingly, ML BlueP is expected to be a promising candidate as a 2D channel material for electronic and optoelectronic devices.

In an actual device with 2D semiconductor material as the channel, metal electrodes are usually in direct contact with the channel owing to the absence of controllable and sustainable substitutional doping methods for ultrathin 2D material. Such metal-2D semiconductor material contacts are often associated with the formation of a finite Schottky barrier, which reduces the carrier injection efficiency [12]. Therefore, decreasing the Schottky barrier height (SBH) in order to form low-resistance metal-2D semiconductor contacts is the greatest challenge because the high Schottky barrier could mask the excellent intrinsic electronic properties of the 2D material. However, the electron/hole SBH does not simply rely on the difference between the Fermi level (E_f) of the metal electrode and the conduction band minimum (CBM)/valence band maximum (VBM) of the intrinsic channel material (such a method used to estimate the SBH Φ_W^e / Φ_W^h is referred to as the work function approximation). This is because of possible Fermi level pinning (FLP) in the metal-semiconductor interface originating from the coupling between the electrode and channel. A more reliable method to evaluate SBH involves the use of a quantum transport simulation based on the two-probe model, where the coupling between the electrode and channel is considered.

It is well established that a strong FLP leads to a robust SBH, while a weak FLP leads to a voltage-tunable SBH [13, 14]. Therefore, the SBH could be reduced by the voltage gate in the case of a weak FLP. To eliminate the interfacial states and reduce the FLP at the 2D semiconductor interfacial contact due to the weak van der Waals (vdW) interaction between them, possible approaches include inserting hexagonal boron nitride (BN) between the 2D semiconductor and the metal electrode [15, 16], as well as utilizing the alloyed 2D metal-semiconductor atomic layer junction [17, 18], surface engineered 2D metal [19], and phase-engineered contacts for 2D materials [20, 21]. In addition, the use of graphene as an electrode is expected to decrease the interfacial states and the FLP for the same reason [14, 22, 23].

In this study, for the first time, we investigate systematically the interfacial properties of the ML BlueP with metal spanning a wide work function range (Sc, Ag, Pt, Pd and Au) in a FET configuration. To do this, we use *ab initio* electronic structure calculations and quantum transport simulations. Owing to band hybridization, there is no Schottky barrier in the vertical direction between the ML BlueP and metal, which are in contact with each other. The quantum transport simulations reveal that an n-type lateral Schottky contact is formed between ML BlueP and Sc, Ag, and Pt electrodes, and that a p-type lateral Schottky contact is formed between ML BlueP and Au and Pd electrodes. A strong FLP is revealed with a pinning factor of 0.42, and this is due to the metal-induced gap states (MIGS). The MIGS between the channel ML BlueP and ML BlueP under the metal electrode region are eliminated by inserting ML graphene between ML BlueP and the metal electrode.

2 Computational details

We used six layers of metal atoms (Au, Ag, Pt, and Pd) as a substrate to construct an interface between ML BlueP and metals. According to convergence tests performed in previous studies [24–26], six layers of metal atoms can represent a real metal substrate. The $\sqrt{3}\times\sqrt{3}$ ML BlueP is adsorbed on top of the (111) surfaces with a 2 × 2 unit cell of Au, Ag, Pt, or Pd, or the 1 × 1 ML BlueP contacts the (0001) surface with a 1 × 1 unit cell of Sc. The pristine lattice parameter of ML BlueP is a = 3.272 Å, which is in good agreement with previous reports [5, 27]. We set the lattice constants of metals as their experimental values and changed the lattice constant of the BlueP layer to the in-plane lattice constants of metals. The mismatches of the lattice constant are 0.5%–3.0%, as listed in Table 1. A vacuum space of at least 16 Å is set perpendicular to the surface to avoid the spurious interaction between periodic units. The binding energy E_b of the ML BlueP–metal interface is defined as $E_b = (E_P + E_M - E_{P+M})/N$, where E_P, E_M, and E_{P+M} are the relaxed energy for pristine ML BlueP, the pure metal surface, and the contact system, respectively. N is the total number of phosphorus atoms that are at the lower layer of ML BlueP in a supercell, as shown in Fig. 1(a).

Table 1 Calculated interfacial properties of ML BlueP on the metal surfaces. ε is the lattice mismatch between the metal and ML BlueP, d_Z is the equilibrium separation of ML BlueP from various metals in the z direction, $d_{P\text{-}M}$ is the minimum P–metal atom-to-atom distance, and E_b is the average energy (per contact P atom) required to remove BlueP sheet from the metal surface. $W_{S\text{-}M}$ is the calculated work function for the metal surface absorbed by ML BlueP, while $\Phi^e_{L,W}$ / $\Phi^h_{L,W}$ and $\Phi^e_{L,T}$ / $\Phi^h_{L,T}$ are the lateral electron/hole SBHs obtained from the work function approximation and the quantum transport simulation, respectively

Metal	ε (%)	d_z (Å)	$d_{P\text{-}M}$ (Å)	E_b (eV)	$W_{S\text{-}M}$ (eV)	Work function app.		Transport method	
						$\Phi^e_{L,W}$ (eV)	$\Phi^h_{L,W}$ (eV)	$\Phi^e_{L,T}$ (eV)	$\Phi^h_{L,T}$ (eV)
Sc	–0.5	1.87	2.67	1.44	4.13	0.16	1.79	0.22	1.62
Ag	–1.9	2.46	2.55	0.22	4.21	0.24	1.71	0.22	1.47
Pt	2.1	1.99	2.24	0.96	4.38	0.41	1.54	0.80	1.30
Pd	3.0	1.97	2.23	1.03	4.80	0.83	1.12	1.02	0.79
Au	–1.7	2.42	2.43	0.20	4.90	0.93	1.02	1.05	0.61

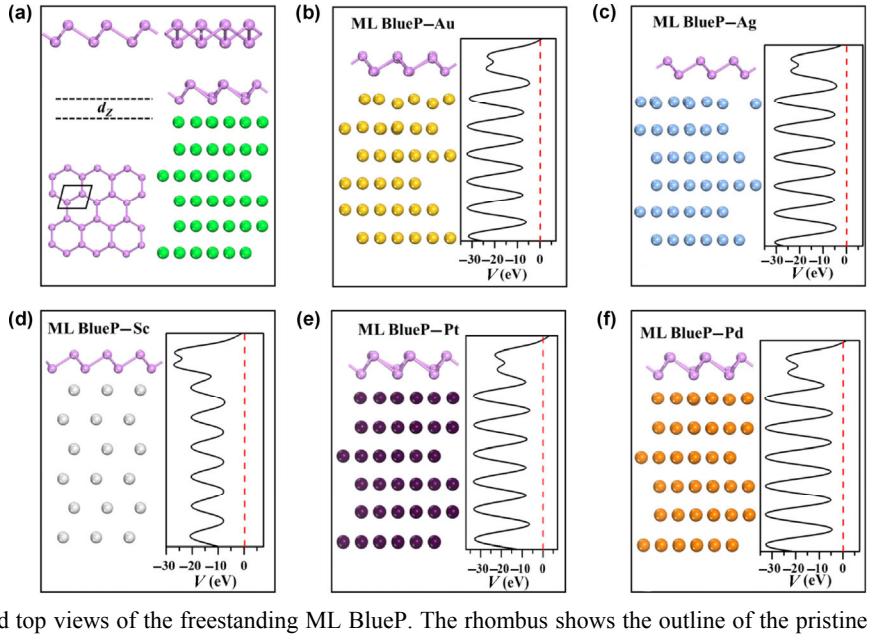

Figure 1 (a) Side and top views of the freestanding ML BlueP. The rhombus shows the outline of the pristine unit cell of ML BlueP. The right side is the illustration of ML BlueP (purple balls) on the metal surface (green balls). (b)–(f) Side views of the optimized structures and average electrostatic potentials in planes normal to the interface of ML BlueP–Au, Ag, Sc, Pt, and Pd systems, respectively. The Fermi level is set to zero.

Geometry optimization is carried out using the projector-augmented wave (PAW) pseudopotential [28, 29] and a plane-wave cut-off energy of 400 eV implemented in the Vienna *ab initio* simulation package (VASP) code [29–33]. The exchange–correlation functional is treated under the GGA of the Perdew–Burke–Ernzerhof (PBE) form [34]. We adopted the semi-empirical dispersion correction scheme (DFT-D2) to take into account the interlayer vdW interaction. We used a Γ-centered grid of 7 × 7 × 1 and 20 × 20 × 1 *k*-points to sample the Brillouin zone [32] in the structural optimization and electronic property calculations, respectively. To obtain reliable optimized structures, the maximum force is less than 10^{-2} eV/Å per atom, and energies are converged to within 10^{-5} eV between two successive steps. During the calculations, the shapes of the supercells and the three bottom metal layers remained constant.

The optimum configurations of the ML BlueP–metal interfaces are shown in Figs. 1(b)–1(f). The structure of ML BlueP is almost preserved on Au, Ag, Sc, Pt, and Pd electrodes. The parameters of ML BlueP–metal contact systems are listed in Table 1. A large d_Z usually corresponds to a large $d_{P\text{-}M}$. The ML BlueP–Sc contact has a large $d_{P\text{-}M}$ of 2.67 Å, but a small d_Z of 1.87 Å. The result is different in the (0001) crystal plane of Sc based on the four other types of metal surfaces, which orientate in the (111) direction.

A two-terminal model of an ML BlueP transistor (Fig. 2) is built with 5-nm ML BlueP as the channel and the contacted interfaces (the ML BlueP–metal interfaces) as electrodes. According to our experiences in previous works [25, 26, 35], a 5-nm channel is sufficient to present SBHs of 2D semiconductor FETs. The lengths of the left and right electrodes are semi-infinite. We calculated the transmission spectrums and local device density of states (LDDOS) using DFT coupled with the non-equilibrium Green's function (NEGF) method, which are implemented in the Atomistix ToolKit (ATK) 2016 package [36–39]. The transmission coefficient $T^{k_{//}}(E)$ ($k_{//}$ is a reciprocal lattice vector point along a surface-parallel direction (orthogonal to the transmission direction) in the irreducible Brillouin zone (IBZ)) and is calculated as

$$T^{k_{//}}(E) = \mathrm{Tr}[\Gamma_L^{k_{//}}(E) G^{k_{//}}(E) \Gamma_R^{k_{//}}(E) G^{k_{//}\dagger}(E)] \quad (1)$$

here, $G^{k_{//}}$ is the retarded (advanced) Green's function and $\Gamma_{L/R}^{k_{//}}(E) = i(\Sigma_{L/R}^{r,k_{//}} - \Sigma_{L/R}^{a,k_{//}})$ represents the level broadening due to the left electrodes and the right electrodes expressed in terms of the electrode self-energies $\Sigma_{L/R}^{k_{//}}$, which reflects the influence of the electrodes on the scattering region [40]. The transmission function at a given energy $T(E)$ is averaged over different $k_{//}$ in the IBZ. We employed a double-ζ polarized (DZP) basis set. The real-space mesh cutoff is 180 Rydberg [10], and the temperature is set at 300 K. We calculated the electronic structures of electrodes and the central region with a Monkhorst–Pack [32] 50 × 1 × 50 and 50 × 1 × 1 *k*-point grid, respectively. We used periodic-type, Neumann-type, and Dirichlet-type boundary conditions [41] in the *x*, *y*, and *z* directions of the device (see Fig. 2), respectively. For the *y*-directions, we chose the Neumann boundary condition, which corresponds to a zero electric field at the boundary of the computational box, and this gives the best model for studying the effect of the gate potential. In the *z*-direction, the boundary condition for the electrostatic potential is determined by the electrostatic potential in the electrodes, corresponding

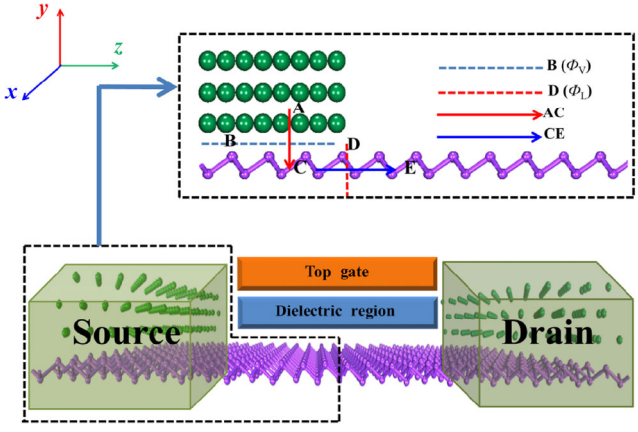

Figure 2 Schematic diagram of an ML BlueP transistor. The contact region of the electrode and channel is zoomed in the top rectangle black dashed line. Top: schematic cross-sectional view of a typical metal contact with the intrinsic ML BlueP channel. The *x*, *y*, and *z* axes are the period direction, the direction vertical to the ML BlueP plane, and the direction along the channel length, respectively. A, C, and E are the three charge transfer (electron/hole-transfer) regions. B and D are the source/drain interface (blue dashed lines) and the source/drain-channel interface D (red dashed lines), respectively. Φ_V and Φ_L represent the vertical SBH and lateral SBH, respectively.

to a Dirichlet boundary condition. A GGA of the PBE form [34] to the exchange-correlation functional is applied in both electronic structure calculations [4] and quantum transport simulations. Many body effects have been significantly depressed in a metal–semiconductor interface structure and a FET configuration owing to the screening of the electron–electron interaction by doped carriers, and the single-electron approximation is thus a good approximation. Taking ML/bilayer/trilayer BP as examples, the measured transport gaps are 1.00/0.71/0.61 eV [4], while the respective calculated DFT-GGA band gaps of pristine phosphorene are 1.11/0.81/0.66 eV [25, 42–44].

3 Results and discussion

3.1 Electronic structure of the ML BlueP–metal interface

In a 2D semiconductor Schottky barrier FET, the Schottky barrier position depends on the interaction strength between the metal and semiconductor. If the contacted 2D semiconductor undergoes metallization owing to a strong interaction with the metal electrode, a Schottky barrier appears at the lateral source/drain-channel interface D (referred to as a lateral Schottky barrier), as shown in Fig. 2. If the band structure of the contacted 2D semiconductor can be identified owing to a weak interaction with the metal electrode, a Schottky barrier appears both at the vertical source/drain interface B (referred to as vertical Schottky barrier) and at the lateral interface D, with the potential for different SBHs. Recently, this Schottky barrier classification has been adopted in the study of MoS_2, graphdiyne, BP, $MoSe_2$, WSe_2, WTe_2, stanene, bismuthene, and arsenene in contact with metal in a FET configuration [2, 25, 26, 43–50].

First, we focus on the isolating ML BlueP–metal interface in the vertical direction. The optimum configurations of the ML BlueP–metal interfaces are shown in Figs. 1(b)–1(f). The structure of ML BlueP is almost preserved on Au, Ag, Sc, Pt, and Pd electrodes. The parameters of ML BlueP–metal contact systems are listed in Table 1. d_Z is the average distance between the ML BlueP and the topmost-layer metal in the vertical direction, as shown in Fig. 1(a). $d_{P\text{-}M}$ is the minimum P–metal atom-to-atom distance in the monolayer blue phosphorene/metal contacts. A large d_Z usually corresponds to a large $d_{P\text{-}M}$. The ML BlueP–Sc contact has a large $d_{P\text{-}M}$ of 2.67 Å, but a small d_Z of 1.87 Å. The results are different in the (0001) crystal plane of Sc based on the four other types of metal surfaces, which orientate in the (111) direction.

According to E_b and d_Z, two categories of adsorption are classified: (1) Au and Ag form relative weak bonds with ML BlueP, with a smaller E_b of 0.20–0.22 eV and a large $d_{P\text{-}M}$ of 2.42–2.46 Å. (2) Sc, Pt and Pd form strong bonds with ML BlueP with a large E_b of 1.03–1.44 eV and a small d_Z of 1.87–1.99 Å. E_b in the BlueP–Pd contact (1.03 eV) is similar to that in the BlueP–Pd contact (0.85 eV). The E_b values in both the BlueP–Au (0.20 eV) and the BlueP–Ag contacts (0.22 eV) are about half the values of the BlackP-Au (0.46 eV) and BlueP–Ag (0.43 eV) [25] contacts. Our E_b of the BlueP–Au contact is comparable with or slightly smaller than the previously calculated ones of 0.31–0.54 eV/atom in terms of the same definition [11, 51].

Next, we explain the difference in the binding energy in terms of the different number of covalent bonds between metal and ML BlueP. The isolate Ag ($4d^{10}5s^1$) and Au atom ($5d^{10}6s^1$) have one unpaired outermost s electron, and form one covalent bond with ML BlueP, even if in the solid form, corresponding to the smallest E_b. The isolate Pd ($4d^{10}$), Sc ($3d^14s^2$), and Pt ($5d^96s^1$) atoms have zero, one, and two unpaired electrons in the open d-shell, respectively. However, according to the Mulliken population analysis, the electrons of the transition metal atoms are redistributed between nd and (n+1)s shells when forming a solid because the d-shells of the transition metal atoms overlap with the significantly broadened p and s shells. Actually, the 4d-shell of Pd loses electrons, and the valence 5s and 5p shells obtain electrons in the solid state. The actual electronic distribution of Pd in the solid state becomes similar to that of Pt. Hence, Pd and Pt atoms form two covalent bonds with ML BlueP in the solid form, corresponding to the medium E_b. The actual electronic configuration of Sc in the solid state becomes approximately $3d^24s^1$, which has three unpaired electrons and forms three covalent bonds with ML BlueP, corresponding to the largest E_b.

As shown in Fig. 3(a), pure ML BlueP is an indirect

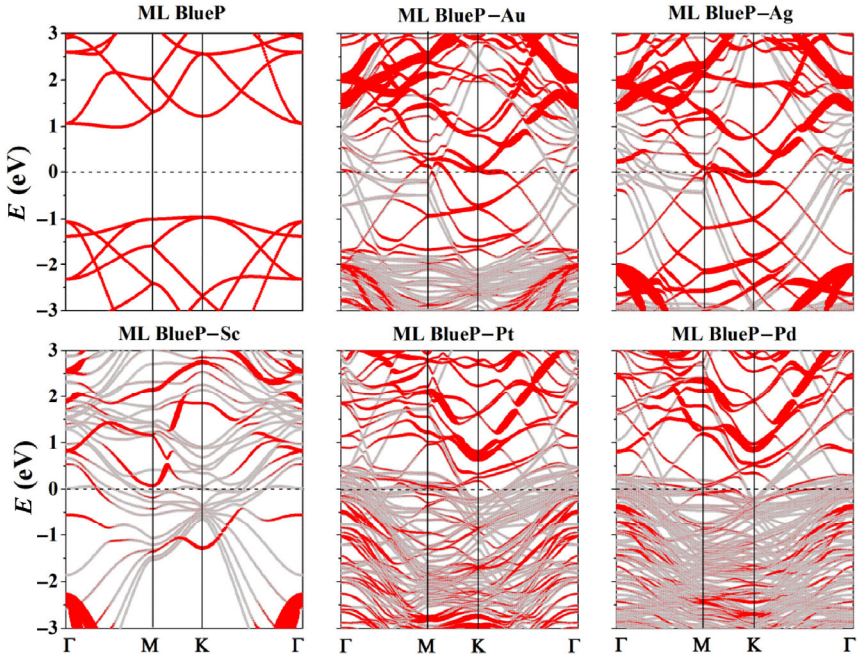

Figure 3 Band structures of the ML BlueP–metal contact systems. Gray lines represent the band structures of the ML BlueP–metal contacts. Red lines represent the band structures projected on ML BlueP, with the line width proportional to the weight. The band structure of the freestanding ML BlueP is calculated based on a $\sqrt{3}\times\sqrt{3}$ supercell. The Fermi level is set as zero energy.

semiconductor with a band gap of 1.83 eV, which is consistent with the previous DFT result of 1.98 eV [5]. The band structures of ML BlueP in contact with Au, Ag, Sc, Pd, and Pt electrodes are shown in Figs. 3(b)–3(f). The red lines represent the bands contributed from P atoms. The band structures of ML-BlueP are destroyed on all the metal electrodes because of the strong band hybridization. The strong band hybridization indicates the formation of chemical bonding between ML BlueP and these metals surfaces, which is consistent with the binding strength. The Fermi level always crosses the band that is contributed from the ML BlueP, indicating the metallization of ML BlueP. The degrees of band hybridization of ML BlueP on the Au and Ag surfaces are weaker than those on the Sc, Pd, and Pt surfaces, which is consistent with the difference in their binding strengths.

To confirm the metallization of ML BlueP absorbed on metals, we calculated the partial density of states (PDOS) on the P orbitals for ML BlueP–metal systems, as shown in Fig. 4. Large amounts of P states appear in the original band gap of ML BlueP in all the absorption systems, leading to a large PDOS of ML BlueP at E_f on the five metal surfaces, which is a typical criterion of metallization. Similar to the ML BP, which is weakly bonded with Ag and Au surfaces [25], the s, p_x, p_y, and p_z orbitals of P contribute almost equally to the states near E_f when ML BlueP is on the surfaces of Ag and Au. In the case of strong bonding, p_z and s orbitals of P dominate the states near E_f in the system where ML BlueP is in contact with Pd (Pt), while the p_y and p_x orbitals of P dominate the states near E_f in the system where ML BlueP is in contact with Sc.

To evaluate the interactions between ML BlueP and metal, we show the electron-density distribution of both the P atoms and metal atoms in real space in Fig. 5 and we present information about bond orders. The electrons are accumulated at the interface between the Au (Ag, Pd and Pt) and ML BlueP in Figs. 5(b) and 5(c) and Figs. 5(e) and 5(f), suggesting the formation of covalent bonds. More electrons are accumulated at the ML BlueP–Pd and ML BlueP–Pt interfaces than at the ML BlueP–Ag and ML BlueP–Au interfaces, which is in agreement with the binding strength and the band hybridization degree. However, the electron accumulation at the Sc–BlueP interface is not as apparent as with other contacts. The bond orders of

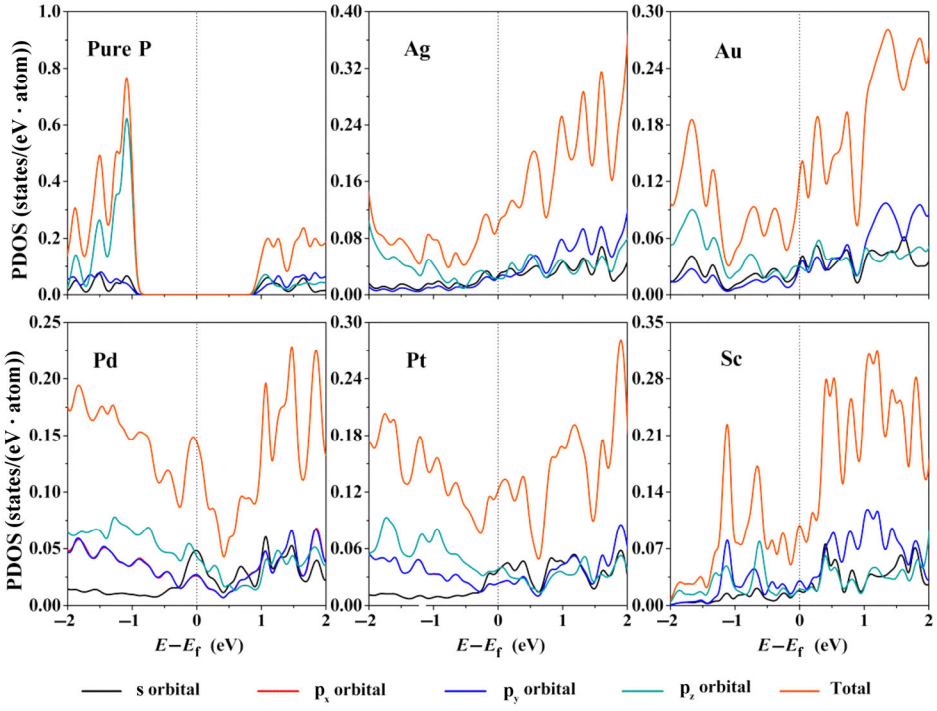

Figure 4 PDOS of pure ML BlueP and ML BlueP on the Ag, Au, Pd, Pt, and Sc surfaces. The Fermi level is set to zero. The PDOS of pure ML BlueP is calculated based on a primitive unit cell. The components of p_x and p_y are identical because of the *C*3 symmetry of ML BlueP.

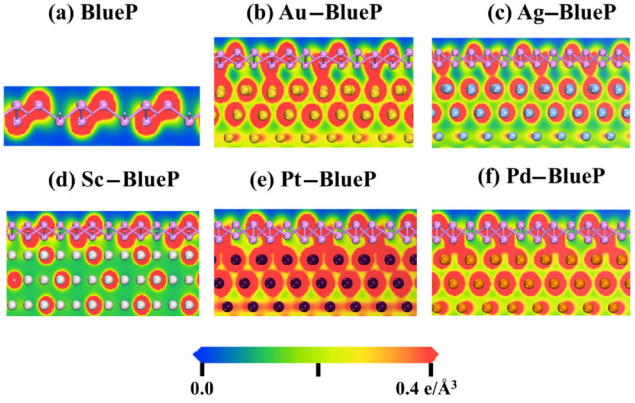

Figure 5 Total electron density distributions of pristine ML BlueP (a) and ML BlueP in contact with (b) Au, (c) Ag, (d) Sc, (e) Pt, and (f) Pd.

P–Ag, Au, Pd, and Pt are 0.38, 0.45, 0.48, and 0.59, respectively, which is consistent with the binding energy and the band hybridization degree. However, the bond order of P–Sc (0.54) is not the maximum among all of the examined systems.

To depict the contact polarity of the ML BlueP–Sc/Ag/Au/Pt/Pd interface, we illustrate the differences in their charge densities in Figs. S1(a)–S1(e) in the Electronic Supplementary Material (ESM), which indicates the charge redistribution at the interface and the existence of the ion bond. The coexistence of the ionic bonds with the covalent bonds in the ML BlueP–Sc/Ag/Au/Pt/Pd contacts is responsible for the binding energy for all the systems. The blue (red) regions represent the electron depletion (accumulation). Sc has a contact polarity that is opposite to that of the other metals. More specifically, Sc loses electrons, while the other metals gain electrons. The charge redistribution is much more significant for the Pd and Pt contact than for the other three metal contacts, and the charge redistribution for the Sc contact is the weakest one.

Next, we investigate the possible formation of a Schottky barrier in the vertical direction by analyzing the band structures of the ML BlueP–metal interfacial systems. According to our analysis, all of the ML BlueP–metal interfaces that were studied are metallized. The metallization band structure reflects the absence of the Schottky barrier in the vertical direction of interface B (as shown in Fig. 2), and the whole ML BlueP–metal composite system may be equivalent to a metal electrode. Consequently, the Schottky barrier of the ML BlueP transistor with the Sc, Ag, Pt, Pd,

and Au electrodes would appear in the lateral direction (interface D), which can be calculated by quantum transport simulations based on the two-probe model.

3.2 Lateral Schottky barrier of the ML BlueP transistors with metal electrodes

The use of quantum transport simulations is a reliable approach to determine the SBH of the ML BlueP transistor owing to the inclusion of the coupling between the electrode and channel. It has been validated in ML, bilayer, and trilayer BP FETs using Ni electrodes [25, 43, 44]. The hole SBHs of the quantum transport simulation (0.26/0.19/0.20 eV) are consistent with the experimental hole SBHs (0.35/0.23/0.21 eV) of ML/bilayer/trilayer BP transistors. By contrast, based on experimental results, the popular work function approximation, where the lateral SBH of a 2D material FET is obtained by evaluating the difference between the E_f values of the metallized 2D material and the CBM (VBM) of the free-standing 2D material, gives completely different hole SBHs of 0.02/–0.10/–0.28 eV. This results from a lack of awareness of the possible coupling between the channel and electrode.

LDDOS is a direct method of reflecting the real space energy-band distribution in FETs, and the LDDOS of ML BlueP transistors with the Sc, Ag, Pt, Pd, and Au electrodes are shown in Figs. 6(a)–6(e), respectively. We show half of the LDDOS spectrums owing to the symmetrical structure of the zero-bias device. The lateral electron SBHs ($\Phi^{e}_{L,T}$) of the ML BlueP–Ag/Sc/Pt transistors are determined from the difference between E_f and the CBM of the channel ML BlueP at the interface, and are given by 0.22, 0.22, and 0.80 eV, respectively. Meanwhile, the lateral hole SBHs ($\Phi^{h}_{L,T}$) of the ML BlueP–Pd/Au transistors are determined from the difference between E_f and the VBM of the channel ML BlueP at the interface, and are given by 0.79 and 0.61 eV, respectively. The transport gap is defined by the sum of the lateral electron SBH ($\Phi^{e}_{L,T}$) and the lateral hole SBH ($\Phi^{h}_{L,T}$): $E^{T}_{g} = \Phi^{e}_{L,T} + \Phi^{h}_{L,T}$, the E^{T}_{g} values of ML BlueP with Sc, Ag, Pt, Pd, and Au electrodes are 1.84, 1.69, 2.10, 1.81, and 1.66 eV, respectively, which are comparable with the calculated band gap of 1.95 eV. The carrier type and the height of the Schottky barrier obtained from the LDDOS calculation are consistent with those obtained from the transmission spectrum calculation (determined from the difference between E_f and the CBM/VBM in the transmission spectrum), as shown in Figs. 6(f)–6(j), because there is a slight band bending of the

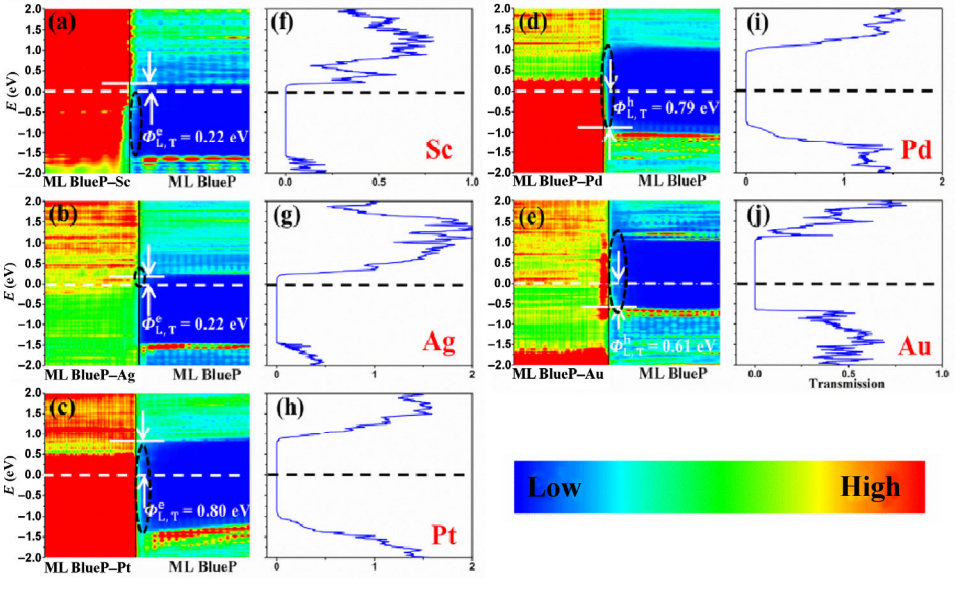

Figure 6 (a)–(e) Zero-bias and zero-gate voltage LDDOS and (f)–(j) transmission spectrums of the ML BlueP transistor with a channel length of L = 5 nm. The MIGS are encircled by a black dashed line. The Fermi level is represented by a white dashed line in (a)–(e) or a black dashed line in (f)–(j). $\Phi^{e}_{L,T}$ and $\Phi^{h}_{L,T}$ respectively represent the electron SBH and hole SBH in the lateral direction. The upright black lines indicate the boundary of the ML BlueP–bulk metal and the uncontacted ML BlueP channel. The color scale is shown below the plot.

channel ML BlueP. Apparent interfacial states appear at the interfaces, with the exception of the Ag electrode, and they are identified as MIGS [13, 52–54].

3.3 Fermi level pinning

The SBH is closely associated with the FLP. First, we determined the FLP between the metallized ML BlueP and the channel ML BlueP by comparing the lateral SBH obtained from the work function approximation and the quantum transport simulations, and combining the density of the MIGS. In Fig. 7(a), we compare the lateral electron/hole SBHs of the ML BlueP obtained from the work function approximation results ($\Phi^{e}_{L,W}/\Phi^{h}_{L,W}$) and the quantum transport simulations ($\Phi^{e}_{L,T}/\Phi^{h}_{L,T}$). There are clear differences in the lateral electron/hole SBHs for Pt, Pd, and Au electrodes, and the contact polarity is the opposite for Pd and Au electrodes. This indicates a strong coupling or a strong FLP between the metallized ML BlueP by Pt, Pd, and Au electrodes and the channel ML BlueP. The observed apparent MIGS at the three interfaces is responsible for such a strong FLP.

The difference in the electron SBH is small for Sc and Ag electrodes, but there are apparent MIGS at the interface between the metallized ML BlueP caused by the Sc electrode and ML channel BlueP. The density of the MIGS at the interface between the metallized ML BlueP caused by the Sc electrode and the channel ML BlueP is comparable with those between the metallized ML BlueP caused by the Pt/Pd/Au electrode and the channel ML BlueP; this indicates a similar degree of FLP. The small difference in the SBH between the two methods is attributed to a small difference in the E_f between the metallized ML BlueP caused by the Sc electrode and the MIGS. A weak coupling or FLP is identified between the metallized ML BlueP caused by the Ag electrode and ML channel BlueP, in that no apparent MIGS appear at the interface between the metallized ML BlueP caused by the Ag electrode and the channel ML BlueP, and because of the small

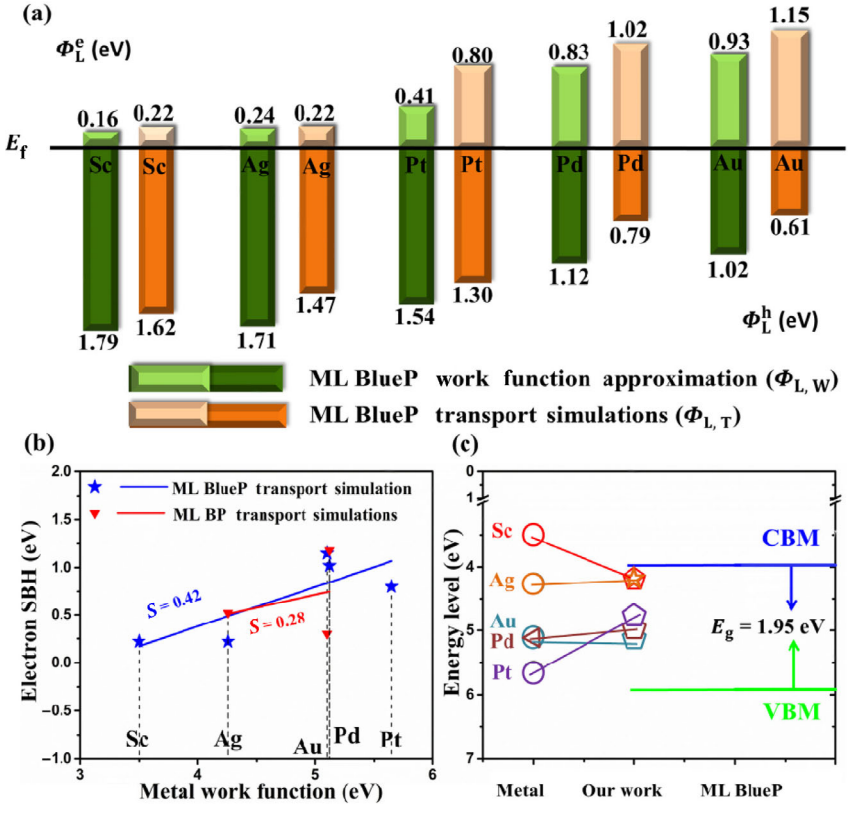

Figure 7 (a) Comparison of the lateral SBHs obtained from the work function approximation calculations and the quantum transport simulations for the ML BlueP transistors. (b) Variation in lateral electron SBHs for the ML BlueP and ML BP transistors with the metal work function. (c) Illustration of FLP in the ML BlueP transistor. *S* is the pinning factor obtained from the Schottky−Mott rule.

difference in the SBH between the two methods.

We adopted pinning factor S to qualitatively describe the degrees of FLP, which are defined as the slope $S = \mathrm{d}\Phi^{\mathrm{e}} / \mathrm{d}W_{\mathrm{M}}$, where W_{M} is the work function of pure metal. S varies from $S = 1$ for an unpinned contact to $S = 0$ for a completely pinned contact, originating from the Schottky–Mott rule [13, 55]. In this paper, we calculate the pinning factor in the terms as $S = \mathrm{d}\Phi^{\mathrm{e}}_{\mathrm{L,T}} / \mathrm{d}W_{\mathrm{M}}$. As shown in Fig. 7(b), we have $S = 0.42$ for ML BlueP, implying a statistically strong FLP between BlueP and metals. This value is slightly higher than the calculated $S = 0.28$ of ML BP [25] and $S = 0.27$ of ML MoS_2 [35, 54]. An illustration of the FLP for ML BlueP in a FET configuration is shown in Fig. 7(c).

The performance of the metal–2D semiconductor contact transistors is limited by the presence of the Schottky barrier, which is difficult to reduce in the case of a strong FLP at the contact interface [56–58]. In contrast, the weak FLP at the metal–semiconductor interface results in a gate-voltage tunable SBH, and thus a significant improvement in the device performance parameters, including the contact resistance, on/off ratios, drive currents, and extrinsic field-effect mobility [13, 17, 18, 59]. Given that our simulated ML BlueP–Ag transistor also has a weak FLP at the interface, it is possible to have a gate-voltage tunable SBH, low contact resistance, and better device performance compared with the other examined ML BlueP–Sc/Pt/Pd/Au transistors.

To prove that the gate voltage can better control the lateral SBH of transistors with weak FLP, we applied a gate voltage to the ML BlueP–Sc transistor, which represents a transistor with a strong FLP, and to the ML BlueP–Ag transistor, which represents a transistor

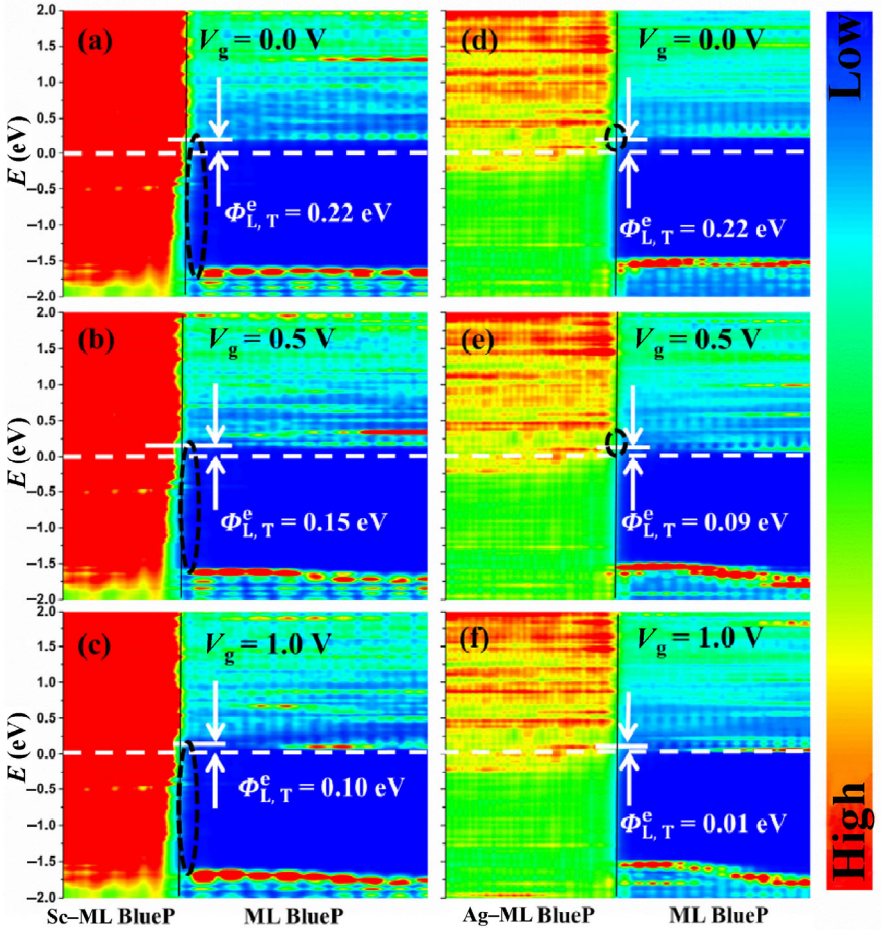

Figure 8 (a)–(f) Zero-bias LDDOS of the ML BlueP transistors with Sc (a)–(c) and Ag (d)–(f) electrodes as a function of the gate voltages. The Fermi level is represented by a white dashed line. The upright black lines indicate the boundary of the ML BlueP–bulk metal and the uncontacted ML BlueP channel. The MIGS are encircled by a black dashed line. The color scale is shown on the right of the plot.

with weak FLP. Both of the two transistors have the lateral electron SBHs of $\Phi^{e}_{L,T}$ = 0.22 eV at zero-bias and zero-gate voltage (shown in Figs. 8(a) and 8(b)). The LDDOS of the ML BlueP–Sc transistor and the ML BlueP–Ag transistor at zero-bias and different gate voltages (V_g = 0.5 and 1.0 V) are compared in Figs. 8(c)–8(f). $\Phi^{e}_{L,T}$ of the ML BlueP–Sc transistor is reduced to 0.15 and 0.10 eV at V_g = 0.5 and 1.0 V, respectively, while $\Phi^{e}_{L,T}$ of the ML BlueP–Ag transistor is reduced to 0.09 and 0.01 eV at V_g = 0.5 and 1.0 V, respectively. To describe the influence of the voltage gate on SBH, we define a gate voltage-dependent SBH reduction rate α (change of SBH from 0 to 1.0 V gate voltage/SBH at 0 V gate voltage ratio). Obviously, α of the ML BlueP–Ag transistor (0.21 eV/V) is higher than that of the ML BlueP–Sc transistor (0.12 eV/V) owing to the weak FLP of the ML BlueP–Ag contact. The ML BlueP–Ag transistor would have the lowest contact resistance and highest performance among the checked five ML BlueP transistors because it has the lowest and most tunable electron SBH.

Considering the contact polarity and degree of the FLP (as shown in Figs. 9(a)–9(c)), we classified the investigated metal-contacted ML BlueP transistors into three categories. The ML BlueP transistor with the Ag electrode forms a Type 1 transistor with an n-type Schottky barrier and weak FLP. The ML BlueP transistor with the Sc/Pt electrode forms a Type 2 transistor with an n-type Schottky barrier and strong FLP. The ML BlueP transistor with the Pd/Au electrode forms a Type 3 transistor with a p-type Schottky barrier and strong FLP. For all three transistors, there is no vertical electron/hole SBH at the interface B, and the electron/hole SBH exists at the metallized ML BlueP and the channel ML BlueP.

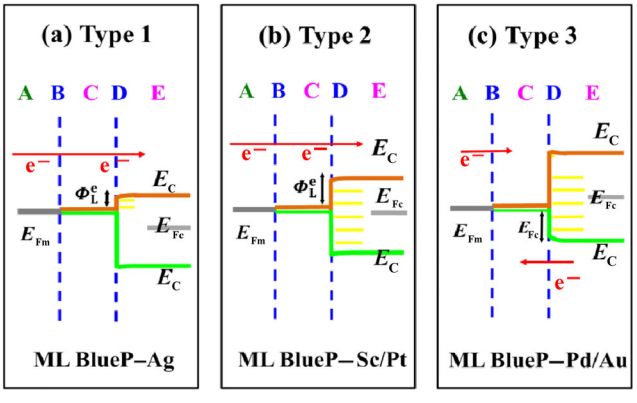

Figure 9 (a)–(c) Three possible band-type schematic diagrams of the ML BlueP–metal transistors. Examples are given at the bottom of each diagram. A, B, C, D, and E represent the different regions or interfaces depicted in Fig. 1. E_{Fm} and E_{Fc} denote the Fermi levels of the absorbed system and intrinsic channel ML BlueP, respectively. E_c and E_v are the conduction band and the valence band of ML BlueP, respectively. Red arrows indicate the flow of electrons or holes. The yellow line represents the MIGS.

3.4 Elimination of the Fermi level pinning

Recent experimental studies and theoretical calculations indicate that the weak FLP could be formed at the 2D semiconductor-2D metal interface, because such an interface has a weak interaction, which leads to the suppression of MIGS [13, 14, 17, 18, 20–23]. We inserted ML hexagonal BN/graphene between the ML BlueP and the Sc surface, and the optimized structure of the ML BlueP–BN/graphene–Sc system is shown in Figs. 10(a) and 10(b). The spacing of the layer increases from 1.87 Å (without inserting the layer) to 3.15/3.48 Å (with the inserted BN/graphene layer), which is comparable with the typical distance of the vdW interaction (3.2–3.5 Å) [60]. The metallized ML BlueP is restored to a semiconducting state (as shown in Figs. 10(c)–10(e)) owing to the weak vdW interaction between ML BN/graphene and ML BlueP. The vertical electron SBH ($\Phi^{e}_{V,B}$) is determined from the difference between E_f and the CBM of ML BlueP obtained from the band structure in Figs. 10(d) and 10(e). Most strikingly, the n-type ohmic contact and quasi ohmic contact with ($\Phi^{e}_{V,B}$) = 0.02 eV are realized in the vertical direction for ML BN and graphene insertion, respectively, with a small number of MIGS in terms of the PDOS shown in Fig. S2 in the ESM.

We illustrate the average electrostatic potentials normal to the interface of the ML BlueP–BN–Sc and the ML BlueP–graphene–Sc systems in Fig. 10(a) and (b), respectively. The tunneling barrier height (TBH) is measured from the Fermi level. Compared with the ML BlueP–Sc interface (Fig. 1(d)) (TBH = –12.67 eV), the ML BlueP–BN–Sc and the ML BlueP–graphene–Sc systems have a larger tunneling barrier at the interface (TBH = 0.27/1.62 eV for BN/graphene insertion) in Figs. 10(a) and 10(b). Namely, the insertion of graphene and BN enhances the tunneling barrier at the vertical

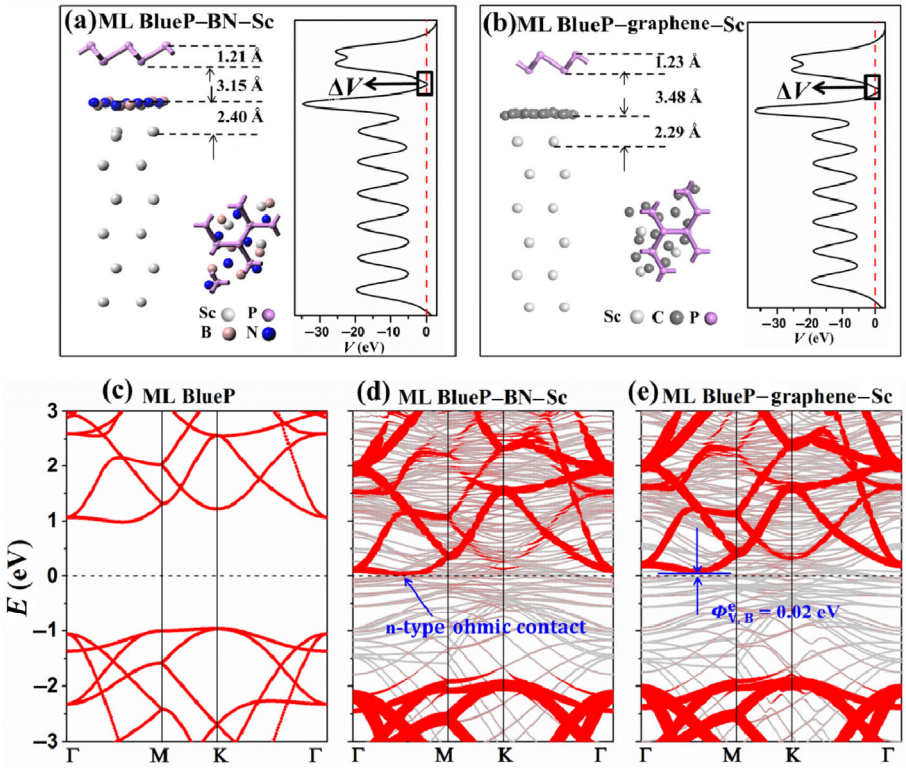

Figure 10 Side views of the optimized structures and average electrostatic potentials in planes normal to the interface of (a) the ML BlueP–BN–Sc and (b) the ML BlueP–graphene–Sc systems. ΔV represents the tunneling barrier. The band structures of the (c) ($\sqrt{3}\times\sqrt{3}$) free-standing ML BlueP, (d) ML BlueP–BN–Sc system, and (e) ML BlueP–graphene–Sc system. Gray line in (c)–(e): band structure of the interfacial systems; Red line in (c)–(e): band structures projected to P atoms. The line width is proportional to the weight. The Fermi level is set at zero energy and is denoted by black dashed lines.

interface. However, according to our calculation, both the tunneling barrier and vertical Schottky barrier with graphene insertion are higher than those with BN insertion.

Although there is a vertical ohmic or quasi ohmic contact at the ML BlueP–BN/graphene–Sc interface (interface B) obtained from its band structure, it is interesting to determine whether such an ohmic or quasi ohmic contact remains in a FET configuration (Fig. 11(a)). The LDDOS of ML BlueP with ML BN/graphene–Sc hybrid electrodes is shown in Figs. 11(b) and 11(c). Surprisingly, a p-type Schottky contact is formed with a large lateral hole SBH of $\Phi^{h}_{L,T}$ = 0.89 eV in the ML BlueP transistor with an ML BN–Sc hybrid electrode (Fig. 11(b)), which is different from that of the ML BlueP transistor with an Sc electrode with respect to the Schottky contact type and SBH. In contrast, the electron SBH of the ML BlueP–graphene–Sc is $\Phi^{e}_{L,T}$ = 0.17 eV (Fig. 11(c)), which is slightly lower than that of the ML BlueP–Sc transistor ($\Phi^{e}_{L,T}$ = 0.22 eV).

The absence of an ohmic or quasi ohmic contact in a ML BlueP transistor configuration with ML BN and graphene insertion reflects the charge redistribution after the channel is introduced. We consider how the real space-band structure of ML BlueP is distributed after the charge redistribution, and we therefore plot the LDDOS that is projected on the ML BlueP in the electrode and the channel regions of the ML BlueP transistor with the ML BN/graphene–Sc hybrid electrode in Figs. 11(d) and 11(e). The n-type vertical ohmic contact remains in the electrode region far from the lateral interface in Fig. 11(d). However, the bands upward clearly bend when approaching the lateral interface, resulting in a large lateral electron SBH. There are apparent MIGS in the lateral metal–semiconductor interface. These MIGS accept electrons not only from ML BlueP approaching the lateral

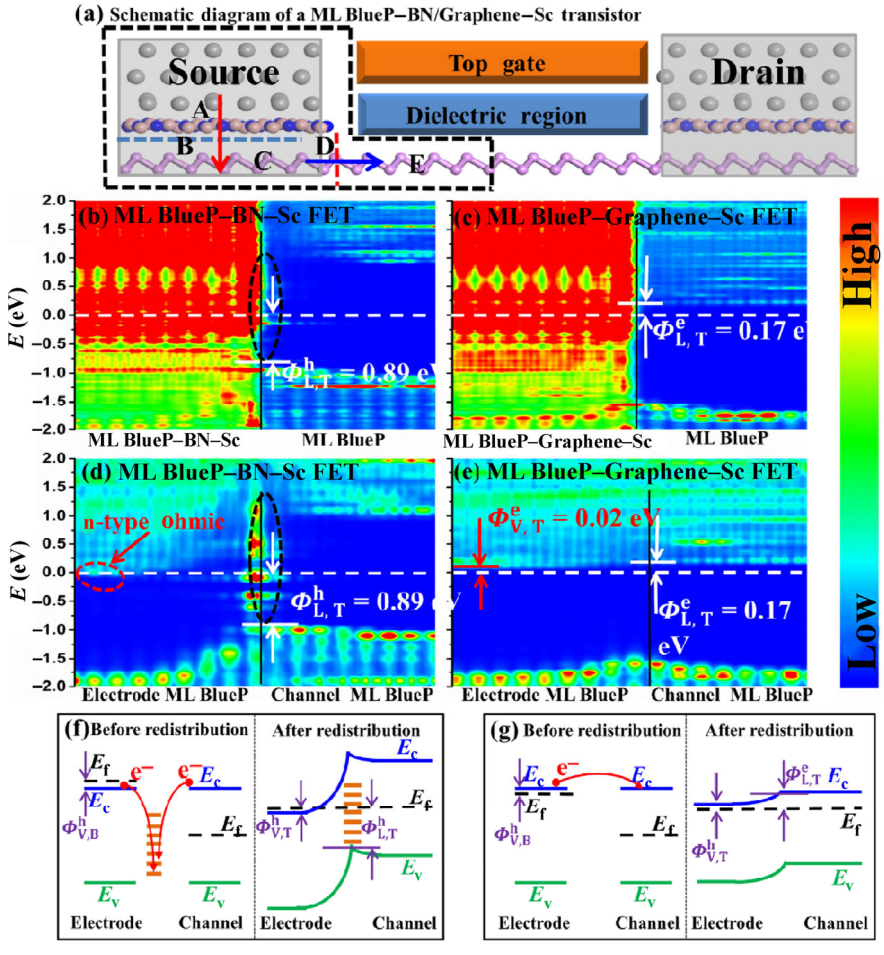

Figure 11 (a) Schematic diagram of an ML BlueP–BN/graphene–Sc transistor. A, C, and E are the three charge-transfer (electron/hole-transfer) regions. B is the vertical interface, and D is the lateral interface. (b) and (c) Zero-bias and zero-gate voltage LDDOS of the ML BlueP–BN–Sc (b) and the ML BlueP–graphene–Sc transistors (c) with a channel length of L = 5 nm. (d) and (e) Same as (b) and (c), respectively, but projected on ML BlueP. (f) and (g) An illustration of the band formation in (d) and (e), respectively. The upright black lines indicate the boundary of the ML BlueP–bulk metal and the uncontacted ML BlueP channel. The MIGS is encircled by a black dashed line. The ohmic contact is circled by a red dashed line. The Fermi level is set as zero. The color scale is shown on the right of the plot.

interface in the electrode region, but also from ML BlueP in the channel region, causing the upward band bending of ML BlueP in the electrode region and channel region. Therefore, E_f is strongly pinned to an energy of 0.89 eV above the VBM of ML BlueP. The band schematic diagrams before and after charge redistribution of the ML BlueP–BN–Sc transistor are compared in Fig. 11(f).

Likewise, an n-type vertical quasi ohmic contact $\Phi^{e}_{L,T}$ = 0.02 eV remains in the electrode region, which is determined from the difference between the E_f and the CBM of ML BlueP in the electrode region far from the lateral interface in Fig. 11(e). The band bends slightly upward when approaching the lateral interface, resulting in a small lateral electron SBH of $\Phi^{h}_{L,T}$ = 0.17 eV. The slight band bending for ML BlueP in the electrode region is attributed to the electron transfer from ML BlueP in the electrode region to the channel ML BlueP because the E_f of the former is higher than that of the latter (in the middle of the gap). Compared with the ML BN insertion scenario, there are few MIGS in the lateral metal–semiconductor interface to serve as reservoirs for electrons in the graphene case. The band schematic diagrams before and after the charge redistribution of the ML BlueP–graphene–Sc transistor are compared in Fig. 11(g). The difference between BN and graphene insertion originates from the very poor screening of insulating

ML BN to the MIGS than metallic ML graphene. As shown in Fig. 8, the weak FLP would give rise to a more tunable SBH, and thus the ML BlueP FET with the ML graphene–Sc hybrid electrode is expected to have a better device performance than that with the Sc electrode and ML BN–Sc hybrid electrode.

4 Conclusions

We provide the first comprehensive study of the interfacial properties of ML BlueP transistors with Sc, Ag, Pt, Pd, and Au electrodes in a FET configuration by using *ab initio* energy-band calculations and quantum transport simulations. ML BlueP on the Sc, Ag, Au, Pd, and Pt surfaces undergoes metallization, and there is no Schottky barrier in the vertical direction. ML BlueP forms strong lateral n-type Schottky contact with Sc and Ag, and weak lateral n-type Schottky contact with Pt electrodes. Further, it forms weak lateral p-type Schottky contact with Au and Pd electrodes owing to the strong FLP, which is exhibited by a pinning factor of 0.42. The MIGS in the ML BlueP–Ag and ML BlueP–graphene–Sc transistors are significantly depressed, leading to a reduced FLP and a better gate-voltage tunability. Unlike ML BP, which favors p-type Schottky contact with metal electrodes [4, 7, 9, 59, 61], ML BlueP prefers n-type Schottky contact with metal electrodes. A combination of n-type ML BlueP transistors and p-type ML BP transistors has potential in the design of complementary metal oxide semiconductors (CMOS).

Acknowledgements

This work was supported by the National Natural Science Foundation of China (Nos. 11274016, 11474012, 11674005, 11274233, and 11664026), the National Basic Research Program of China (Nos. 2013CB932604 and 2012CB619304), Ministry of Science and Technology (National Materials Genome Project) of China (Nos. 2016YFA0301300 and 2016YFB0700600), and Foundation of Henan Educational Committee (No. 17A430026).

Electronic Supplementary Material: Supplementary material (charge density difference of ML BlueP–metal interface and PDOS of pure ML BlueP and ML BlueP on the ML BN/graphene–Sc surfaces) is available in the online version of this article at https://doi.org/10.1007/s12274-017-1801-2.

References

[1] Fiori, G.; Bonaccorso, F.; Iannaccone, G.; Palacios, T.; Neumaier, D.; Seabaugh, A.; Banerjee, S. K.; Colombo, L. Electronics based on two-dimensional materials. *Nat. Nanotechnol.* **2014**, *9*, 768–779.

[2] Kang, J. H.; Liu, W.; Sarkar, D.; Jena, D.; Banerjee, K. Computational study of metal contacts to monolayer transition-metal dichalcogenide semiconductors. *Phy. Rev. X* **2014**, *4*, 031005.

[3] Schwierz, F.; Pezoldt, J.; Granzner, R. Two-dimensional materials and their prospects in transistor electronics. *Nanoscale* **2015**, *7*, 8261–8283.

[4] Das, S.; Zhang, W.; Demarteau, M.; Hoffmann, A.; Dubey, M.; Roelofs, A. Tunable transport gap in phosphorene. *Nano Lett.* **2014**, *14*, 5733–5739.

[5] Guan, J.; Zhu, Z.; Tománek, D. Phase coexistence and metal-insulator transition in few-layer phosphorene: A computational study. *Phys. Rev. Lett.* **2014**, *113*, 046804.

[6] Xiao, J.; Long, M. Q.; Zhang, X. J.; Ouyang, J.; Xu, H.; Gao, Y. L. Theoretical predictions on the electronic structure and charge carrier mobility in 2D phosphorus sheets. *Sci. Rep.* **2015**, *5*, 9961.

[7] Liu, H.; Neal, A. T.; Zhu, Z.; Luo, Z.; Xu, X. F.; Tománek, D.; Ye, P. D. Phosphorene: An unexplored 2D semiconductor with a high hole mobility. *ACS Nano* **2014**, *8*, 4033–4041.

[8] Li, L. K.; Yu, Y. J.; Ye, G. J.; Ge, Q. Q.; Ou, X. D.; Wu, H.; Feng, D. L.; Chen, X. H.; Zhang, Y. B. Black phosphorus field-effect transistors. *Nat. Nanotechnol.* **2014**, *9*, 372–377.

[9] Buscema, M.; Groenendijk, D. J.; Blanter, S. I.; Steele, G. A.; van der Zant, H. S. J.; Castellanos-Gomez, A. Fast and broadband photoresponse of few-layer black phosphorus field-effect transistors. *Nano Lett.* **2014**, *14*, 3347–3352.

[10] Zhu, Z.; Tománek, D. Semiconducting layered blue phosphorus: A computational study. *Phys. Rev. Lett.* **2014**, *112*, 176802.

[11] Zhang, J. L.; Zhao, S. T.; Han, C.; Wang, Z. Z.; Zhong, S.; Sun, S.; Guo, R.; Zhou, X.; Gu, C. D.; Yuan, K. D. et al. Epitaxial growth of single layer blue phosphorus: A new phase of two-dimensional phosphorus. *Nano Lett.* **2016**, *16*, 4903–4908.

[12] Allain, A.; Kang, J. H.; Banerjee, K.; Kis, A. Electrical contacts to two-dimensional semiconductors. *Nat. Mater.* **2015**, *14*, 1195–1205.

[13] Liu, Y. Y.; Stradins, P.; Wei, S. H. Van der Waals metal-semiconductor junction: Weak Fermi level pinning enables

effective tuning of Schottky barrier. *Sci. Adv.* **2016**, *2*, e1600069.

[14] Quhe, R.; Peng, X. Y.; Pan, Y. Y.; Ye, M.; Wang, Y. Y.; Zhang, H.; Feng, S. Y.; Zhang, Q. X.; Shi, J. J.; Yang, J. B. et al. Can a black phosphorus Schottky barrier transistor be good enough? *ACS Appl. Mater. Interfaces* **2017**, *9*, 3959–3966.

[15] Wang, J. L.; Yao, Q.; Huang, C. W.; Zou, X. M.; Liao, L.; Chen, S. S.; Fan, Z. Y.; Zhang, K.; Wu, W.; Xiao, X. H. et al. High mobility MoS_2 transistor with low Schottky barrier contact by using atomic thick h-BN as a tunneling layer. *Adv. Mater.* **2016**, *28*, 8302–8308.

[16] Farmanbar, M.; Brocks, G. Controlling the Schottky barrier at MoS_2/metal contacts by inserting a BN monolayer. *Phys. Rev. B* **2015**, *91*, 161304.

[17] Chuang, H. J.; Chamlagain, B.; Koehler, M.; Perera, M. M.; Yan, J. Q.; Mandrus, D.; Tománek, D.; Zhou, Z. X. Low-resistance 2D/2D ohmic contacts: A universal approach to high-performance WSe_2, MoS_2, and $MoSe_2$ transistors. *Nano Lett.* **2016**, *16*, 1896–1902.

[18] Kim, A. R.; Kim, Y.; Nam, J.; Chung, H. S.; Kim, D. J.; Kwon, J. D.; Park, S. W.; Park, J.; Choi, S. Y.; Lee, B. H. et al. Alloyed 2D metal-semiconductor atomic layer junctions. *Nano Lett.* **2016**, *16*, 1890–1895.

[19] Liu, Y. Y.; Xiao, H.; Goddard III, W. A. Schottky-barrier-free contacts with two-dimensional semiconductors by surface-engineered MXenes. *J. Am. Chem. Soc.* **2016**, *138*, 15853–15856.

[20] Cho, S.; Kim, S.; Kim, J. H.; Zhao, J.; Seok, J.; Keum, D. H.; Baik, J.; Choe, D. H,; Chang, K. J.; Suenaga, K. et al. Phase patterning for ohmic homojunction contact in $MoTe_2$. *Science* **2015**, *349*, 625–628.

[21] Kappera, R.; Voiry, D.; Yalcin, S. E.; Branch, B.; Gupta, G.; Mohite, A. D.; Chhowalla, M. Phase-engineered low-resistance contacts for ultrathin MoS_2 transistors. *Nat. Mater.* **2014**, *13*, 1128–1134.

[22] Liu, Y.; Wu, H.; Cheng, H. C.; Yang, S.; Zhu, E. B.; He, Q. Y.; Ding, M. N.; Li, D. H.; Guo, J.; Weiss, N. O. et al. Toward barrier free contact to molybdenum disulfide using graphene electrodes. *Nano Lett.* **2015**, *15*, 3030–3034.

[23] Avsar, A.; Vera-Marun, I. J.; Tan, J. Y.; Watanabe, K.; Taniguchi, T.; Neto, A. H. C.; Özyilmaz, B. Air-stable transport in graphene-contacted, fully encapsulated ultrathin black phosphorus-based field-effect transistors. *ACS Nano* **2015**, *9*, 4138–4145.

[24] Wang, Y. Y.; Li, J. Z.; Xiong, J. H.; Pan, Y. Y.; Ye, M.; Guo, Y.; Zhang, H.; Quhe, R.; Lu, J. Does the Dirac cone of germanene exist on metal substrates? *Phys. Chem. Chem. Phys.* **2016**, *18*, 19451–19456.

[25] Pan, Y. Y.; Wang, Y. Y.; Ye, M.; Quhe, R.; Zhong, H. X.; Song, Z. G.; Peng, X. Y.; Yu, D. P.; Yang, J. B.; Shi, J. J. et al. Monolayer phosphorene–metal contacts. *Chem. Mater.* **2016**, *28*, 2100–2109.

[26] Pan, Y. Y.; Li, S. B.; Ye, M.; Quhe, R.; Song, Z. G.; Wang, Y. Y.; Zheng, J. X.; Pan, F.; Guo, W. L.; Yang, J. B. et al. Interfacial properties of monolayer $MoSe_2$–metal contacts. *J. Phys. Chem. C* **2016**, *120*, 13063–13070.

[27] Li, Y. C.; Chen, X. B. Dirac fermions in blue-phosphorus. *2D Mater.* **2014**, *1*, 031002.

[28] Blöchl, P. E. Projector augmented-wave method. *Phys. Rev. B* **1994**, *50*, 17953–17979.

[29] Kresse, G.; Joubert, D. From ultrasoft pseudopotentials to the projector augmented-wave method. *Phys. Rev. B* **1999**, *59*, 1758–1775.

[30] Kresse, G.; Hafner, J. *Ab initio* molecular dynamics for liquid metals. *Phys. Rev. B* **1993**, *47*, 558–561.

[31] Kresse, J.; Furthmüller G. Efficiency of *ab-initio* total energy calculations for metals and semiconductors using a plane-wave basis set. *Comput. Mater. Sci*. **1996**, *6*, 15–50.

[32] Monkhorst, H. J.; Pack, J. D. Special points for Brillouin-zone integrations. *Phys. Rev. B* **1976**, *13*, 5188–5192.

[33] Kresse, G.; Hafner, J. *Ab initio* molecular-dynamics simulation of the liquid-metal–amorphous-semiconductor transition in germanium. *Phy. Rev. B* **1994**, *49*, 14251–14269.

[34] Perdew, J. P.; Burke, K.; Ernzerhof, M. Generalized gradient approximation made simple. *Phys. Rev. Lett.* **1996**, *77*, 3865–3868.

[35] Zhong, H. X.; Quhe, R.; Wang, Y. Y.; Ni, Z. Y.; Ye, M.; Song, Z. G.; Pan, Y. Y.; Yang, J. B.; Yang, L.; Lei, M. et al. Interfacial properties of monolayer and bilayer MoS_2 contacts with metals: Beyond the energy band calculations. *Sci. Rep.* **2016**, *6*, 21786.

[36] Brandbyge, M.; Mozos, J. L.; Ordejón, P.; Taylor, J.; Stokbro, K. Density-functional method for nonequilibrium electron transport. *Phys. Rev. B* **2002**, *65*, 165401.

[37] Smith, D. R.; Schultz, S.; Markoš, P.; Soukoulis, C. M. Determination of effective permittivity and permeability of metamaterials from reflection and transmission coefficients. *Phys. Rev. B* **2002**, *65*, 195104.

[38] Soler, J. M.; Artacho, E.; Gale, J. D.; García, A.; Junquera, J.; Ordejón, P.; Sánchez-Portal, A. D. The SIESTA method for *ab initio* order-N materials simulation. *J. Phys.: Condens. Matter* **2002**, *14*, 2745–2779.

[39] *Atomistix ToolKit*, version 2016; QuantumWise A/S: Copenhagen, Denmark, 2017. http://www.quantumwise.com (accessed Jun 9, 2017).

[40] Çakır, D.; Peeters, F. M. Dependence of the electronic and transport properties of metal-$MoSe_2$ interfaces on contact structures. *Phys. Rev. B* **2014**, *89*, 245403.

[41] Cheng, A. H. D.; Cheng, D. T. Heritage and early history of the boundary element method. *Eng. Anal. Bound. Elem.* **2005**, *29*, 268–302.

[42] Qiao, J. S.; Kong, X. H.; Hu, Z. X.; Yang, F.; Ji, W. High-mobility transport anisotropy and linear dichroism in few-layer black phosphorus. *Nat. Commun.* **2014**, *5*, 4475.

[43] Pan, Y. Y.; Dan, Y.; Wang, Y. Y.; Ye, M.; Zhang, H.; Quhe, R.; Zhang, X. Y.; Li, J. Z.; Guo, W. L.; Yang, L. et al. Schottky barriers in bilayer phosphorene transistors. *ACS Appl. Mater. Interfaces* **2017**, *9*, 12694–12705.

[44] Zhang, X. Y.; Pan, Y. Y.; Ye, M.; Quhe, R.; Wang, Y. Y.; Guo, Y.; Dan, Y.; Song, Z. G.; Li, J. Z.; Yang, J. B. et al. Three-layer phosphorene–metal interfaces. *Nano Res.*, in press, DOI: 10.1007/s12274-017-1680-6.

[45] Pan, Y. Y.; Wang, Y. Y.; Wang, L.; Zhong, H. X.; Quhe, R.; Ni, Z. Y.; Ye, M.; Mei, W. N.; Shi, J. J.; Guo, W. L. et al. Graphdiyne-metal contacts and graphdiyne transistors. *Nanoscale* **2015**, *7*, 2116–2127.

[46] Wang, Y. Y.; Yang, R. X.; Quhe, R.; Zhong, H. X.; Cong, L. X.; Ye, M.; Ni, Z. Y.; Song, Z. G.; Yang, J. B.; Shi, J. J. et al. Does p-type Ohmic contact exist in WSe_2-metal interfaces? *Nanoscale* **2016**, *8*, 1179–1191.

[47] Guo, Y.; Pan, F.; Ye, M.; Wang, Y. Y.; Pan, Y. Y.; Zhang, X. Y.; Li, J. Z.; Zhang, H.; Lu, J. Interfacial properties of stanene–metal contacts. *2D Mater.* **2016**, *3*, 035020.

[48] Guo, Y.; Pan, F.; Ye, M.; Sun, X. T.; Wang, Y. Y.; Li, J. Z.; Zhang, X. Y.; Zhang, H.; Pan, Y. Y.; Song, Z. G. et al. Monolayer bismuthene-metal contacts: A theoretical study. *ACS Appl. Mater. Inter.* **2017**, *9*, 23128–23140.

[49] Wang, Y. Y.; Ye, M.; Weng, M. Y.; Li, J. Z.; Zhang, X. Y.; Zhang, H.; Guo, Y.; Pan, Y. Y.; Xiao, L.; Liu, J. K. et al. Electrical contacts in monolayer arsenene devices. *ACS Appl. Mater. Interfaces*, in press, doi: 10.1021/acsami.7b08513.

[50] So, C.; Zhang, H.; Wang, Y. Y.; Ye, M.; Pan, Y. Y.; Quhe, R.; Li, J. Z.; Zhang, X. Y.; Zhou, Y. S.; Lu, J. A computational study of monolayer hexagonal WTe_2 to metal interfaces. *Phys. Status Solidi B*, in press, DOI: 10.1002/pssb.201600837.

[51] Zeng, J.; Cui, P.; Zhang, Z. Y. Half layer by half layer growth of a blue phosphorene monolayer on a GaN(001) substrate. *Phys. Rev. Lett.* **2017**, *118*, 046101.

[52] Heine, V. Theory of surface states. *Phys. Rev.* **1965**, *138*, A1689–A1696.

[53] Gong, C.; Colombo, L.; Wallace, R. M.; Cho, K. The unusual mechanism of partial Fermi level pinning at metal-MoS_2 interfaces. *Nano Lett.* **2014**, *14*, 1714–1720.

[54] Guo, Y. Z.; Liu, D. M.; Robertson, J. 3D behavior of schottky barriers of 2D transition-metal dichalcogenides. *ACS Appl. Mater. Interfaces* **2015**, *7*, 25709–25715.

[55] Kim, C.; Moon, I.; Lee, D.; Choi, M. S.; Ahmed, F.; Nam, S.; Cho, Y.; Shin, H. J.; Park, S.; Yoo, W. J. Fermi level pinning at electrical metal contacts of monolayer molybdenum dichalcogenides. *ACS Nano* **2017**, *11*, 1588–1596.

[56] Liu, H.; Neal, A. T.; Ye, P. D. Channel length scaling of MoS_2 MOSFETs. *ACS Nano* **2012**, *6*, 8563–8569.

[57] Das, S.; Appenzeller, J. WSe_2 field effect transistors with enhanced ambipolar characteristics. *Appl. Phys. Lett.* **2013**, *103*, 103501.

[58] Ling, Z. P.; Sakar, S.; Mathew, S.; Zhu, J. T.; Gopinadhan, K.; Venkatesan, T.; Ang, K. W. Black phosphorus transistors with near band edge contact schottky barrier. *Sci. Rep.* **2015**, *5*, 18000.

[59] Du, Y. C.; Liu, H.; Deng, Y. X.; Ye, P. D. Device perspective for black phosphorus field-effect transistors: Contact resistance, ambipolar behavior, and scaling. *ACS Nano* **2014**, *8*, 10035–10042.

[60] Lebedeva, I. V.; Lebedev, A. V.; Popov, A. M.; Knizhnik, A. A. Comparison of performance of van der Waals-corrected exchange-correlation functionals for interlayer interaction in graphene and hexagonal boron nitride. *Comp. Mater. Sci.* **2017**, *128*, 45–58.

[61] Das, S.; Demarteau, M.; Roelofs, A. Ambipolar phosphorene field effect transistor. *ACS Nano* **2014**, *8*, 11730–11738.